THE JOURNAL OF PHYSICAL CHEMISTRY A
A JOURNAL OF THE AMERICAN CHEMICAL SOCIETY

pubs.acs.org/JPCA Article

Atmospheric Chemistry of $HOHg^{(II)}O^{\bullet}$ Mimics That of a Hydroxyl Radical

Darshi T. Hewa Edirappulige, Ilena J. Kirby, Camille K. Beckett, and Theodore S. Dibble*

Cite This: https://doi.org/10.1021/acs.jpca.3c04159 Read Online

ACCESS | Metrics & More | Article Recommendations | SI Supporting Information

ABSTRACT: $HOHg^{(II)}O^{\bullet}$, formed from $HOHg^{(I)\bullet}$ + O_3, is a key intermediate in the OH-initiated oxidation of $Hg^{(0)}$ in the atmosphere. As no experimental data are available for $HOHg^{(II)}O^{\bullet}$, we use computational chemistry (CCSD(T)//M06-2X/AVTZ) to characterize its reactions with atmospheric trace gases (NO, NO_2, CH_4, C_2H_4, CH_2O and CO). In summary, $HOHg^{(II)}O^{\bullet}$, like the analogous $BrHg^{(II)}O^{\bullet}$ radical, largely mimics the reactivity of $^{\bullet}OH$ in reactions with NO_x, alkanes, alkenes, and aldehydes. The rate constant for its reaction with methane ($HOHg^{(II)}O^{\bullet} + CH_4 \rightarrow Hg^{(II)}(OH)_2 + {}^{\bullet}CH_3$) is about four times higher than that of •OH at 298 K. All of these reactions maintain mercury as $Hg^{(II)}$, except for $HOHg^{(II)}O^{\bullet} + CO \rightarrow HOHg^{(I)\bullet} + CO_2$. Considering only the six reactions studied here, we find that reduction by CO dominates the fate of $HOHg^{(II)}O^{\bullet}$ (79−93%) in many air masses (in the stratosphere and at ground level in rural, marine, and polluted urban regions) with only modest competition from $HOHg^{(II)}O^{\bullet} + CH_4$ (<15%). We expect that this work will help global modeling of atmospheric mercury chemistry.

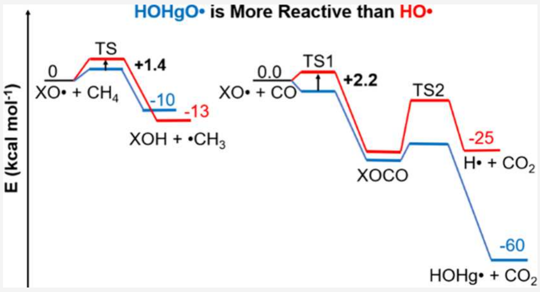

1. INTRODUCTION

Mercury (Hg), a potent neurotoxic pollutant detrimental to both human and environmental health, is emitted to the atmosphere largely in the form of elemental mercury ($Hg^{(0)}$).[1] The concern over Hg in the atmosphere emerges from its deposition into terrestrial and aquatic ecosystems, where it can be converted into methyl mercury (CH_3Hg^+).[2−4] Methyl mercury can be biomagnified through aquatic food chains, leading to high Hg levels in fish consumed by humans. Mercury, especially methyl mercury, is highly neurotoxic and poses a severe risk to human and wildlife health. Elemental mercury is removed from the gaseous atmosphere either by uptake into vegetation, dry deposition to oceans,[5,6] or via oxidation into $Hg^{(II)}$. Unlike $Hg^{(0)}$, $Hg^{(II)}$ compounds are fairly water-soluble and can undergo either wet deposition or dry deposition into oceans.[3,7] As a result, we must gain an understanding of mercury redox chemistry in the gas phase if we are to predict when and where mercury enters ecosystems.[8] Experimental studies of the kinetics and mechanism of gas-phase reactions of $Hg^{(0)}$ face challenges due to surface-catalyzed reactions. Most regional and global models[9−12] of atmospheric Hg assume oxidation occurs irreversibly in reactions with O_3 and OH, where $Hg^{(II)}O$ is the main product (R1 and R2, respectively).[13,14]

$$Hg^{(0)} + O_3 \rightarrow Hg^{(II)}O + O_2 \tag{R1}$$

$$Hg^{(0)} + OH + \{O_2\} \rightarrow Hg^{(II)}O + HO_2 \tag{R2}$$

However, $Hg^{(II)}O$ in the gas phase is so unstable ($D_0 \approx 4$ kcal mol^{-1})[15] that it would dissociate to $Hg^{(0)}$ + O or react with O_2 to make O_3;[16] as a result, no net mercury oxidation would occur. Since 2006, some models of atmospheric mercury oxidation treated $Hg^{(0)}$ oxidation as a two step process initiated by atomic bromine and followed by addition of a radical:[17,18]

$$Br + Hg^{(0)} + M \leftrightharpoons BrHg^{\bullet(I)} + M \tag{R3}$$

$$BrHg^{\bullet(I)} + {}^{\bullet}Y + M \rightarrow BrHg^{(II)}Y + M \tag{R4}$$

where M is another molecule of air and $Y^{\bullet}$ are relatively abundant atmospheric radicals (Y = NO_2, HOO, halogen oxides, etc.). This Br-initiated mechanism is kinetically plausible and explains observations in the marine boundary layer[19−21] and the gas phase chemistry of rapid mercury depletion events in the Artic spring.[22−24] However, field measurements in continental areas are harder to explain without invoking the participation of OH and/or O_3.[21,25] The existence of two sets of models with completely different oxidation mechanisms introduces large uncertainties into efforts to understand of the behavior of atmospheric mercury.[26,27]

More recently, Shah et al.[28] proposed an alternative way to convert $Hg^{(I)}$ to $Hg^{(II)}$, one that may resolve the discrepancies

Received: June 20, 2023
Revised: August 25, 2023

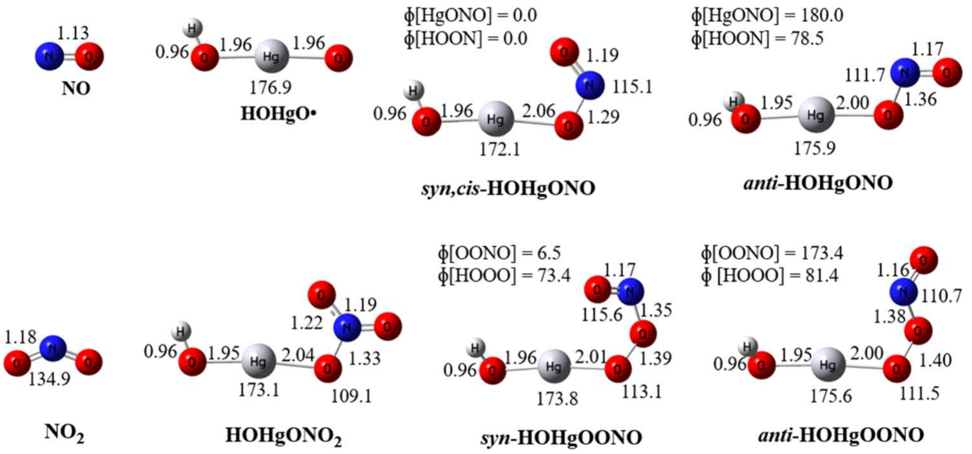

Figure 1. Structures of reactants and products of the reactions $HOHg^{(II)}O^{\bullet}$ + NO and $HOHg^{(II)}O^{\bullet}$ + NO_2 at M06-2X/AVTZ. Angles and bond distances are given in degrees and Å, respectively. $HOHg^{(I)\bullet}$, *syn,cis*-$HOHg^{(II)}ONO$, and $HOHg^{(II)}ONO_2$ possess C_s symmetry, while all other molecules with more than three atoms possess C_1 symmetry.

between the two sets of models. They considered a two-step oxidation mechanism initiated by Br (R3) *or* OH (R5):

$$OH + Hg^{(0)} + M \leftrightarrows HOHg\bullet^{(I)} + M \tag{R5}$$

and concluded by reaction of the $Hg^{(I)}$ intermediate with O_3:[29−31]

$$BrHg^{\bullet(I)} + O_3 \rightarrow BrHg^{(II)}O^{\bullet} + O_2 \tag{R6}$$

$$HOHg^{\bullet(I)} + O_3 \rightarrow HOHg^{(II)}O^{\bullet} + O_2 \tag{R7}$$

The resulting $Hg^{(II)}$ species, $HOHg^{(II)}O^{\bullet}$, has never been characterized by experiment or computational chemistry. In order to guide modelers of atmospheric mercury, we carried out an extensive survey of the atmospheric fate of $HOHg^{(II)}O^{\bullet}$.

Peterson and Balabanov[32] reported that $BrHg^{(II)}O^{\bullet}$ possesses two strong bonds (D_0 = 70 kcal mol^{-1} for Br−HgO and 60 kcal mol^{-1} for BrHg−O), so that it must be stable with respect to dissociation in the gas phase. Given that R6 and R7 possess fairly similar ΔH_r° (42.1 and 47.0 kcal mol^{-1}, respectively),[31] it follows that $HOHg^{(II)}O^{\bullet}$ is thermally stable in the atmosphere, so that its fate is reaction with trace gases.

In the current study, we study reactions of $HOHg^{(II)}O^{\bullet}$ with a range of abundant trace gases (NO, NO_2, CH_4, C_2H_4, CH_2O, and CO):

$$HOHg^{(II)}O^{\bullet} + NO \rightarrow HOHg^{(II)}ONO \tag{R8}$$

$$HOHg^{(II)}O^{\bullet} + NO_2 \rightarrow HOHg^{(II)}ONO_2 \text{ or } HOHg^{(II)}OONO \tag{R9}$$

$$HOHg^{(II)}O^{\bullet} + CH_4 \rightarrow Hg^{(II)}(OH)_2 + {}^{\bullet}CH_3 \tag{R10}$$

$$HOHg^{(II)}O^{\bullet} + C_2H_4 \rightarrow HOHg^{(II)}OCH_2CH_2^{\bullet} \tag{R11}$$

$$HOHg^{(II)}O^{\bullet} + CH_2O \rightarrow Hg^{(II)}(OH)_2 + HCO \tag{R12a}$$

$$HOHg^{(II)}O^{\bullet} + CH_2O \rightarrow HOHg^{(II)}OCH_2O^{\bullet} \tag{R12b}$$

$$HOHg^{(II)}O^{\bullet} + CO \rightarrow HOHg^{\bullet(I)} + CO_2 \tag{R13}$$

Methane, in addition to being abundant in the atmosphere, serves as a model for a wide range of volatile organic compounds (VOCs) containing sp^3-hybridized carbon atoms bound to hydrogen atoms. Ethene is considered as the prototype for alkenes, including isoprene and terpenes, which constitute a large fraction of the mass of VOCs emitted to the atmosphere. We chose formaldehyde as the model compound to represent a range of aldehydes emitted to the atmosphere or produced in photooxidation of VOCs. The relative abundance of NO_x in urban air masses (several parts per billion) and typical [CO] in the atmosphere (~100 ppbv) enhance their potential significance in determining the atmospheric fate of $HOHg^{(II)}O^{\bullet}$.

Immediately below, we discuss the theoretical methods for quantum chemistry and computational kinetics. We then present calculated potential energy profiles (PEPs) for $HOHg^{(II)}O\bullet$ reacting with NO and NO_2. Next, we discuss the energetics and kinetics of the reaction with CH_4. This is followed by presentations of the PEPs for the $HOHg^{(II)}O^{\bullet}$ reaction with C_2H_4, CH_2O, and CO. We estimate rate constants for reactions of $HOHg^{(II)}O^{\bullet}$ with species other than CH_4 by analogy to calculated values for $BrHg^{(II)}O^{\bullet}$. Finally, we evaluate the likely fates of $HOHg^{(II)}O^{\bullet}$ in four specific regions of the atmosphere with respect to the six trace gases considered in this study.

2. METHODS

Quantum chemistry calculations were performed using Gaussian16.[33] Geometries of all stationary points and points along minimum energy paths (MEPs) were optimized using density functional theory (DFT) methods followed by harmonic vibrational frequencies calculations. We used the functionals PBE0 (called PBE1PBE in Gaussian16) and M06-2X as they have performed well for structures, frequencies, and energies in previous studies of mercury compounds.[34−38] For the reaction between $HOHg^{(II)}O^{\bullet}$ and CO, PBE0 did not optimize the prereactive complex, probably because of its poor treatment of dispersion forces.[39] As a result, we rely here on M06-2X structures and frequencies. The standard Dunning's aug-cc-pVTZ[40,41] basis set was used for C, O, N, and H atoms. The relativistic effect of Hg cannot be ignored as it is a heavy atom, so we used the Stuttgart/Cologne pseudopotentials to account for the scalar relativistic effect of the innermost 60 electrons of the Hg atom. The remaining 20 electrons were explicitly treated with the aug-cc-pVTZ (-PP) basis set of Peterson and coworkers.[42−44] The combination of these basis sets is abbreviated as AVTZ. Spin-unrestricted calculations were performed on the

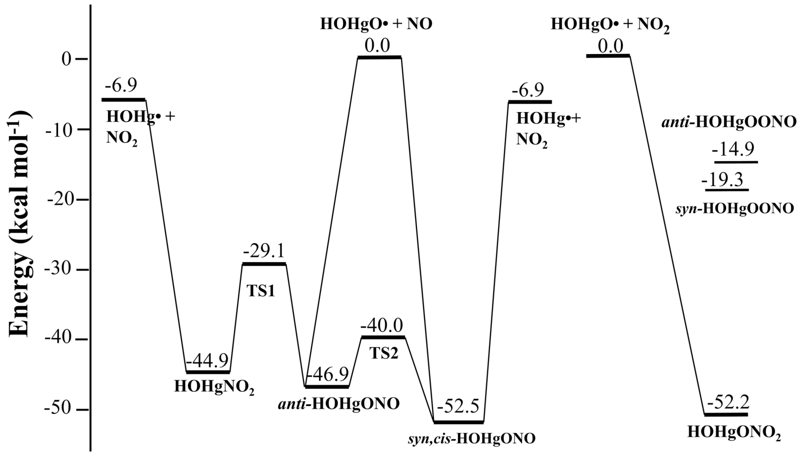

Figure 2. ZPE-corrected potential energy profiles for $HOHg^{(II)}O^{\bullet}$ + NO and $HOHg^{(II)}O^{\bullet}$ + NO_2 at CCSD(T)//M06-2X/AVTZ are from this work. The relative energies of $HOHg^{(II)}NO_2$, $HOHg^{(I)\bullet}$ + NO_2, and the TSs are at CCSD(T)//PBE0/AVTZ.[49]

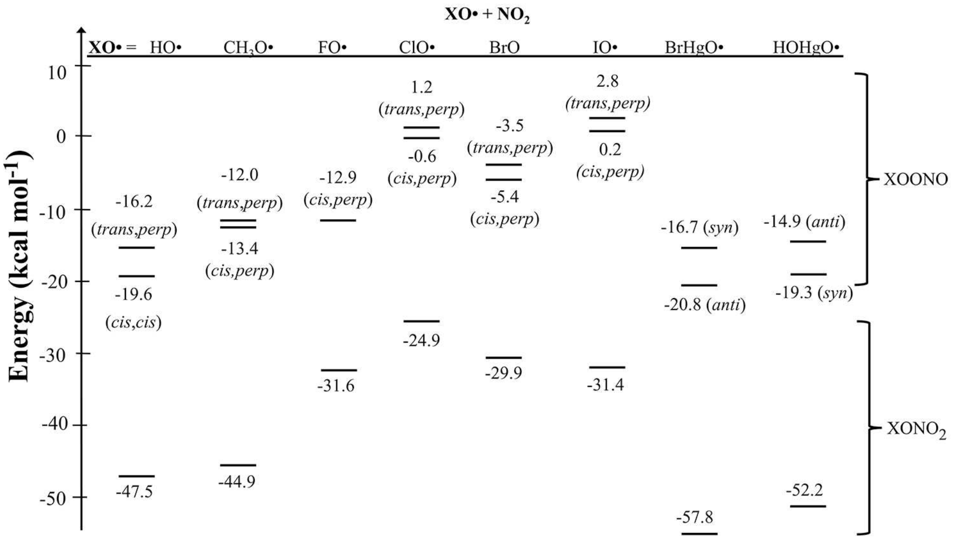

Figure 3. Isomer energies (at 0 K) of possible products for XO radicals reacting with NO_2.[52−55]

radical species. Spin−orbit corrections were ignored as they should be modest for non-radical products and for the O- and O-centered radicals that make up the key species in the chemistry we are exploring.

All calculations in the present work were initially performed without imposing any symmetry. However, if a C_1-symmetric geometry appeared to be close to C_s symmetry (the highest symmetry we found), we symmetrized the structure, reoptimized it, and then recalculated the vibrational frequencies to verify that the C_s structure was a minimum on the potential energy surface.

We checked that reactants and products possessed only real vibrational frequencies and that each transition state had only a single imaginary frequency. The identities of transition states were validated by visualizing the motion of their imaginary frequencies and running intrinsic reaction coordinate (IRC) calculations.

Single-point energy calculations on DFT-optimized geometries were done using coupled cluster single and double excitations with perturbative triples, CCSD(T),[45] along with the AVTZ basis set. The frozen-core approximation was used to correlate only the 5d and 6s electrons of Hg plus the valence electrons of H, C, and N.

Canonical rate constants, $k^{\mathrm{CTST}}(T)$, for the reaction $HOHg^{(II)}O^{\bullet}$ + CH_4 were refined using 1-dimensional variational transition state theory[46,47] for 200 K ≤ T ≤ 325 K. Tunneling corrections were estimated using the asymmetric Eckart potential[48] and incorporated to compute the effective rate constants, $k^{\mathrm{VTST+Eckart}}(T)$.

3. RESULTS AND DISCUSSION

All of the relative energies mentioned in this study are enthalpies at 0 K reported at CCSD(T)//M06-2X/AVTZ, unless otherwise specified.

3.1. Adding NO and NO_2 to $HOHg^{(II)}O^{\bullet}$. $HOHg^{(II)}O^{\bullet}$ can form stable compounds by reaction with NO_x via addition. Figure 1 illustrates the optimized geometries of the reactants and products. In characterizing the dihedral angles for $HOHg^{(II)}ONO$ in Figure 1, *syn* or *anti* refers to ϕ[HgONO] and *cis* or *trans* refers to the ϕ[HOON]. Because the OHgO angle is almost linear in every structure, definitions of dihedral angles around the Hg−O bond are not informative.

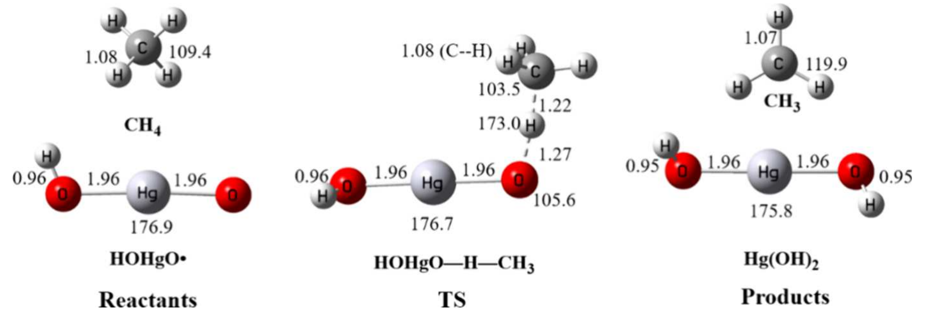

Figure 4. Structures of reactants, products, and saddle point of the $HOHg^{(II)}O^{\bullet}$ + CH_4 reaction at M06-2X/AVTZ. The angles and bond distances are given in degrees and Å, respectively. $HOHg^{(II)}O^{\bullet}$ possesses C_s symmetry, while the transition state (TS) and $Hg^{(II)}(OH)_2$ hold C_1 and C_2 symmetries, respectively.

As shown in Figure 2, the *syn,cis*-$HOHg^{(II)}ONO$ conformer lies 5.6 kcal mol^{-1} below the *anti*-conformer and possesses a $HOHg^{(II)}O$-NO bond energy of 52 kcal mol^{-1}. A *syn,trans* conformer with almost the same energy as *syn,cis*-$HOHg^{(II)}ONO$ was found and optimized with both functionals but had an imaginary frequency at M06-2X/AVTZ (see Table S1). Hence, this conformer was not included in Figures 1 or 2.

$HOHg^{(II)}O^{\bullet}$ reacts with NO_2 to form $HOHg^{(II)}ONO_2$ with a reaction enthalpy of −52 kcal mol^{-1}. These reactants can also produce both *syn* and *anti*-conformers of $HOHg^{(II)}OONO$, but these reaction channels are only exothermic by 19 and 15 kcal mol^{-1}, respectively.

Both *anti*- and *syn*-$HOHg^{(II)}ONO$ form without a barrier from $HOHg^{(II)}O^{\bullet}$ + NO. Isomerization of *anti*-$HOHg^{(II)}ONO$ to *syn*-$HOHg^{(II)}ONO$ requires overcoming a critical energy of 6.9 kcal mol^{-1}. Addition of $HOHg^{(II)}O^{\bullet}$ to NO_2 forms $HOHg^{(II)}ONO_2$ without a barrier (Figure S3). We found saddle points separating both syn and anti conformers of $HOHg^{(II)}OONO$ from reactants. Formation of the anti-conformer will not occur under atmospheric conditions due to its high energy barrier (15.3 kcal mol^{-1}). The transition state for the formation of *syn*-$HOHg^{(II)}OONO$ was found to be submerged with respect to the reactants at CCSD(T)//M06-2X/AVTZ (−1.2 kcal mol^{-1}, versus +3.7 kcal mol^{-1} at M06-2X/AVTZ). Barriers for reactions of prereactive complexes (PRCs) are often submerged (lower in energy than isolated reactants), but in this case, the negative energy appears to arise from a discrepancy between the nature of the potential energy surfaces at M06-2X versus CCSD(T). We were not encouraged to resolve this discrepancy as we expect that *syn*-$HOHg^{(II)}OONO$, like HOONO,[50,51] to rapidly fall apart to reactants, making its formation insignificant. As shown in Figure 3, the much greater stability of $HOHg^{(II)}ONO_2$ than $HOHg^{(II)}OONO$ conforms to the trend for a wide range of $XO^{\bullet}$, including HO, $BrHg^{(II)}O^{\bullet}$, halogen oxides, and alkoxy radicals (RO•).[52,53]

We did not calculate the rate constants for the barrierless addition of NO_x to $HOHg^{(II)}O^{\bullet}$ in the current study due to (a) the uncertainty inherent in DFT calculations; (b) the computational cost of the methods (multireference + dynamical correlation) required to obtain more reliable energies; and (c) the uncertainties in energy transfer parameters necessary to obtain $k(P,T)$. For the present, we suggest (as we did for $BrHg^{(II)}O^{\bullet}$ + NO_x)[38] that the rate constants will be similar to those for $CH_3O^{\bullet} + NO + M \rightarrow CH_3ONO + M$ and $CH_3O^{\bullet} + NO_2 + M \rightarrow CH_3ONO_2 + M$. At 298 K and 1 atm, these correspond to 2.9×10^{-11} and 1.7×10^{-11} molecules cm^{-3} s^{-1}, respectively.[53]

3.2. $HOHg^{(II)}O^{\bullet} + CH_4 \rightarrow Hg^{(II)}(OH)_2 + {}^{\bullet}CH_3$.

$HOHg^{(II)}O^{\bullet}$, like OH and $BrHg^{(II)}O^{\bullet}$, reacts with CH_4 via H atom abstraction.[38] Figure 4 depicts the structures of reactants, products, and the saddle point for the $HOHg^{(II)}O^{\bullet}$ + CH_4 reaction.

As shown in Figure 4, on going from $HOHg^{(II)}O^{\bullet}$ to $Hg^{(II)}(OH)_2$, the OHgO angle becomes more nonlinear by 1.1° and the HO−Hg and Hg−O bond distances change by less than 0.01 Å.

We compared the barrier heights (at saddle points) for hydrogen abstraction from methane by OH using both PBE0 and M06-2X versus highly accurate results by Ellingson et al.[56] (Figure S1). M06-2X agreed with the benchmark results much better than did PBE0. Consequently, we used the energies of the stationary points refined at CCSD(T)//M06-2X/AVTZ to determine the PEP for $HOHg^{(II)}O^{\bullet} + CH_4$. Figure 5 displays the corresponding PEPs for the $XHg^{(II)}O^{\bullet}$ + CH_4 (X = Br, OH) reactions.

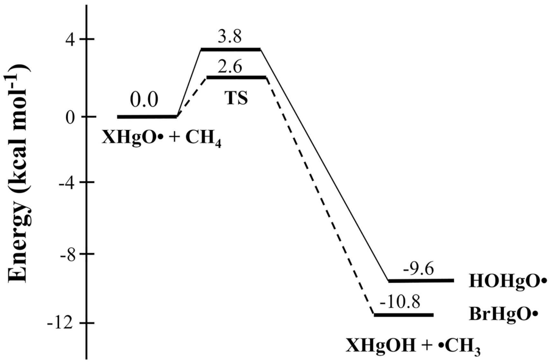

Figure 5. ZPE-corrected potential energy profile for the $BrHg^{(II)}O^{\bullet}$ + CH_4[38] (dashed lines) and $HOHg^{(II)}O$• + CH_4 (solid lines) reactions at CCSD(T)//M06-2X/AVTZ. Relative energies of transition states are given at the saddle points.

The reaction $HOHg^{(II)}O^{\bullet}$ + CH_4 proceeds via a modest energy barrier of 3.8 kcal mol^{-1}. Both this barrier and the energy of the products are 1.2 kcal mol^{-1} higher than those for $BrHg^{(II)}O^{\bullet}$ + CH_4. The final products, $XHg^{(II)}OH$ are thermally stable. While $BrHg^{(II)}OH$ is photolyzed in about a day in the troposphere,[57] the tropospheric photochemistry of $Hg^{(II)}(OH)_2$ remains unclear. The one previous calculation suggests that photolysis occurs slowly in the troposphere due to the high vertical excitation energy (at least 6.3 eV = 197 nm).[58]

Table 1 lists the harmonic vibrational frequencies, integrated intensities, and mode descriptions for $Hg^{(II)}(OH)_2$. Notably, the

Table 1. Vibrational Mode Descriptions, Symmetries, Harmonic Frequencies ($\tilde{\nu}$) from this Work and the Literature, and Integrated Intensities of $Hg^{(II)}(OH)_2$ at M06-2X/AVTZ

		(cm^{-1})			Intensities ($km\ mol^{-1}$)
mode description	symmetry	experiment[a] ref 59	B3LYP ref 59	this work	
O−H wag	A		123	100	105
O−Hg—O bend	B		152	175	5.8
O−Hg—O bend	A		167	180	0.09
Hg−O symmetric stretch	A		541	583	0.05
Hg−O anti-symmetric stretch	B	637, 644	607	640	136
Hg−O—H anti-symmetric bend	B	927, 929	946	921	97
Hg−O—H symmetric bend	A		957	926	8.1
O−H anti-symmetric stretch	B	3629, 3642	3827	3896	119
O−H symmetric stretch	A		3828	3897	18.6

[a] Experimentally observed frequencies given for an argon matrix and then a neon matrix.

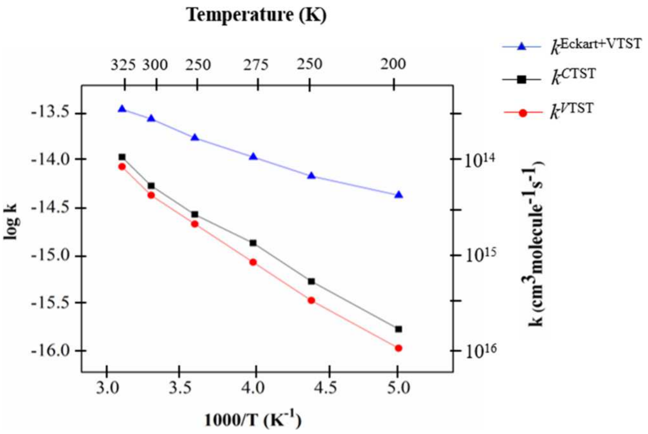

Figure 6. Canonical (k^{CTST}), variational (k^{VTST}), and variational rate constants with Eckart tunneling ($k^{Eckart+VTST}$) in units of (cm^3 $molecule^{-1}$ s^{-1}) for the $HOHg^{(II)}O^{\bullet}$ + CH_4 reaction at CCSD(T)//M06-2X/AVTZ.

Table 2. Temperature Dependence of the Canonical Rate Constant (k^{CTST}), Position of the Variational Transition State Position (s^{VTST}, in a_0), Canonical Rate Constant (k^{CTST}), Variational (k^{VTST}/k^{CTST}) Correction, Eckart Tunneling Correction (κ^{Eckart}), and Best Calculated Rate Constant ($k^{Eckart+VTST}$) for the $HOHg^{(II)}O^{\bullet}$ + CH_4 Reaction at CCSD(T)//M06-2X/AVTZ[a]

T (K)	k^{CTST}	s^{VTST}	k^{VTST}/k^{CTST}	κ^{Eckart}	$k^{(Eckart+VTST)}$
200	1.4×10^{-16}	−0.125	0.66	37.8	3.5×10^{-15}
225	4.6×10^{-16}	−0.104	0.70	18.6	5.9×10^{-15}
250	1.2×10^{-15}	−0.083	0.73	11.1	9.4×10^{-15}
275	2.7×10^{-15}	−0.083	0.75	7.48	1.5×10^{-14}
300	5.4×10^{-15}	−0.062	0.80	5.53	2.4×10^{-14}
325	9.9×10^{-15}	−0.062	0.75	4.35	3.2×10^{-14}

[a] All rate constants possess units of cm^3 $molecule^{-1}$ s^{-1}.

computed harmonic frequencies of 640 and 921 cm^{-1} for the Hg−O bond stretching and Hg−O−H bending agree well with the experimental frequencies of 637 and 927 cm^{-1} reported by Wang et al. (2005) in solid argon.[59]

To determine the $HOHg^{(II)}O-H$ bond dissociation energy (D_0), we considered the same two isodesmic reactions used by Lam et al., (2019)[38] to calculate D_0 of $BrHg^{(II)}O-H$.

$$HOHg^{(II)}O^{\bullet} + H_2O \rightarrow HOHg^{(II)}OH + {}^{\bullet}OH \quad \text{(R14)}$$

$$HOHg^{(II)}O^{\bullet} + CH_3OH \rightarrow HOHg^{(II)}OH + CH_3O^{\bullet} \quad \text{(R15)}$$

We calculated D_0 of $HOHg^{(II)}O-H$ as 113.7 ± 0.1 kcal mol^{-1} by averaging results from R14 and R15 (see Table S5). HO−H and $BrHg^{(II)}O-H$ possess larger D_0 than does $HOHg^{(II)}O-H$ by 3.9 and 0.8 kcal mol^{-1}, respectively.

Figure 6 displays the temperature dependence of the rate constants for $HOHg^{(II)}O^{\bullet}$ + CH_4, while Table 2 lists the canonical rate constant, variational correction, and tunneling correction versus temperature. At 298 K, the rate constant is 2.4×10^{-14} molecules cm^{-3} s^{-1}, approximately 10 times lower than that for $BrHg^{(II)}O^{\bullet}$ + CH_4 and four times higher than that of $OH^{\bullet}$ + CH_4. Tunneling increases the rate constant by factors ranging from 38 at 200 K to 4 at 325 K. The variational effect significantly lowers the rate constants; $k^{VTST}(T)/k^{CTST}(T)$ rises from 0.66 at 200 K to 0.75 at 325 K. The position of the variational transition states, s^{VTST}, is negative at all temperatures, and its position ranges from −0.062 to −0.125 a_0.

3.3. $HOHg^{(II)}O^{\bullet}$ + C_2H_4 → $HOHg^{(II)}OCH_2CH_2^{\bullet}$. We found that $HOHg^{(II)}O^{\bullet}$ readily adds to C_2H_4 via a submerged energy barrier, while hydrogen abstraction from C_2H_4 possesses a critical energy of 3.3 kcal mol^{-1} (Table S9). The structures of reactants, products, and all saddle points for the addition reaction are displayed in Figure 7, while Figure 8 compares the PEPs for $HOHg^{(II)}O^{\bullet}$ + C_2H_4 versus $BrHg^{(II)}O^{\bullet}$ + C_2H_4.[60]

The $HOHg^{(II)}O^{\bullet}$ + C_2H_4 reaction proceeds via a prereactive complex (PRC) before going through a modest energy barrier to form a carbon-centered radical ($HOHg^{(II)}OCH_2CH_2^{\bullet}$). Two conformers of the product were found: the more stable conformer with Φ[HgOCC] = 44° (which we term folded) and the other conformer with Φ[HgOCC] = 176° (termed extended), and both possess C_1 symmetry.

The PEP for the $HOHg^{(II)}O^{\bullet}$ + C_2H_4 system is more complex than that for $HOHg^{(II)}O^{\bullet}$ + CH_4 due to the presence of a PRC and two conformers of the product. The PRCs in $BrHg^{(II)}O^{\bullet}$ + C_2H_4 and $HOHg^{(II)}O^{\bullet}$ + C_2H_4 lie below the separated reactants by 4.7 and 3.7 kcal mol^{-1}, respectively. The saddle point (labeled as TS_{add}) lies 0.5 kcal mol^{-1} above the PRC for both systems.[60] The extended conformer of $HOHg^{(II)}OCH_2CH_2^{\bullet}$ lies approximately 1.6 kcal mol^{-1} above the more stable folded conformer. These two conformers are linked through a rotational saddle point (labeled as TS_{iso}) that lies 1.0 kcal mol^{-1} above the extended conformer. As this PEP is very similar to that observed for $BrHg^{(II)}O^{\bullet}$ + C_2H_4,[60] we make a zeroth-order approximation that they share the same rate constants (~2×10^{-12} cm^3 $molecule^{-1}$ s^{-1}, 200 K ≤ T ≤ 333 K and 0.01 atm ≤ P ≤ 1 atm). However, we suggest that the rate constant for $HOHg^{(II)}O^{\bullet}$ + C_2H_4 is less than that of the $BrHg^{(II)}O^{\bullet}$ + C_2H_4 system on account of the weaker binding of the PRC and the higher relative energy of the saddle point. We did not consume further resources for calculating the rate constant for the $HOHg^{(II)}O^{\bullet}$ + C_2H_4 system.

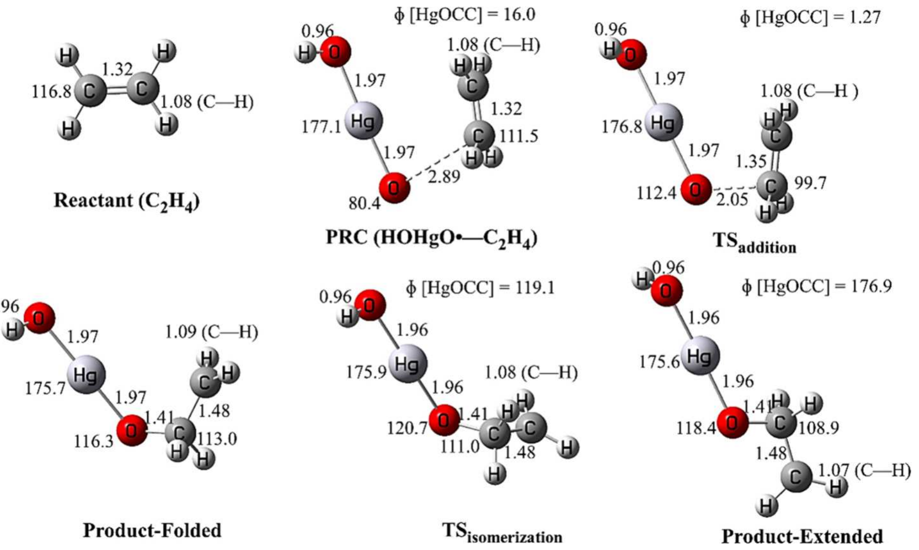

Figure 7. Reactants, products ($HOHgO^{(II)}CH_2CH_2^{\bullet}$ conformers), and saddle points of the $HOHg^{(II)}O^{\bullet}$ + C_2H_4 reaction at M06-2X/AVTZ. The angles and bond distances are given in degrees and Å, respectively. Except for $HOHg^{(II)}O^{\bullet}$ and C_2H_4, all of the species possess C_1 symmetry.

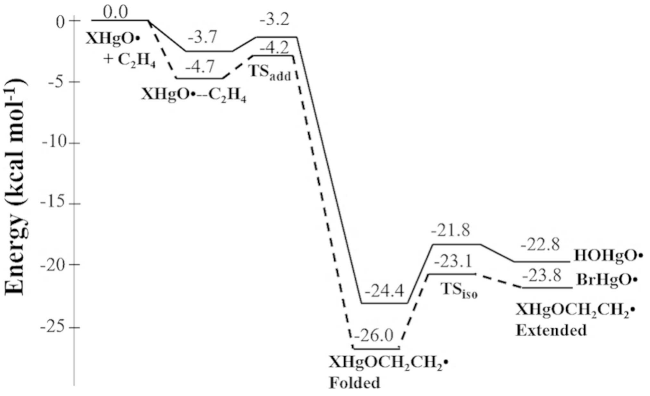

Figure 8. ZPE-corrected potential energy profiles for the $HOHg^{(II)}O^{\bullet}$ + C_2H_4 and $BrHg^{(II)}O^{\bullet}$ + C_2H_4 reactions at CCSD(T)//M06-2X/AVTZ.

3.4. $HOHg^{(II)}O^{\bullet}$ Reactions with CH_2O.

We used CH_2O (formaldehyde) to model the reaction between $HOHg^{(II)}O^{\bullet}$ and aldehydes as a class. Figure 9 depicts the structures of reactants, products, PRCs, and saddle points of the $HOHg^{(II)}O^{\bullet}$ + CH_2O reaction for the most stable conformers of those stationary points. The Supporting Information (see Table S1) provides Cartesian coordinates of less stable conformers.

Like $BrHg^{(II)}O^{\bullet}$, $HOHg^{(II)}O^{\bullet}$ can react with CH_2O by two channels: either by abstracting a hydrogen atom (giving $Hg^{(II)}(OH)_2$ + HCO) or by adding to the carbon atom of CH_2O to produce $HOHg^{(II)}OCH_2O\bullet$. We found two conformers of $HOHg^{(II)}OCH_2O^{\bullet}$, where ϕ[HgOCO] is either 0° (the more stable, included in Figure 9) or 178.6° (Table S1). Each reaction channel includes a PRC, a submerged saddle point ($TS_{abstraction}$ or $TS_{addition}$) and an exothermic product or product set. The two PRCs are linked via a rotational saddle point, labeled $TS_{isomerization}$. The fact that $TS_{addition}$ is submerged

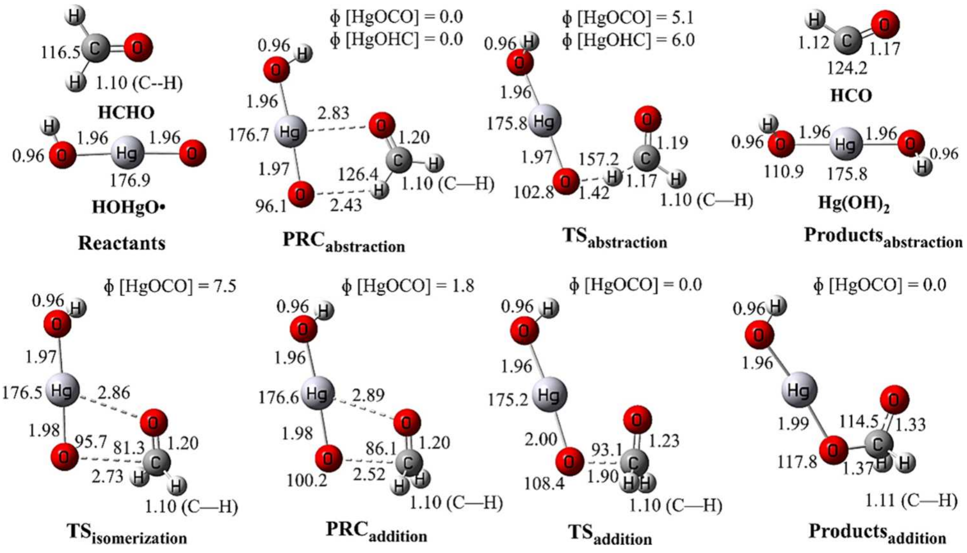

Figure 9. Reactants, products, and saddle points of the $HOHg^{(II)}O^{\bullet}$ + CH_2O reaction (distances in Å, bond angles and dihedral angles in degrees) optimized at M06-2X/AVTZ. $HOHg^{(II)}O^{\bullet}$, $PRC_{abstraction}$, $TS_{addition}$, and $HOHg^{(II)}OCH_2O^{\bullet}$ possess C_s symmetry, and $Hg(OH)_2$ possesses C_2 symmetry. All other mercury species belong to the C_1 point group.

https://doi.org/10.1021/acs.jpca.3c04159

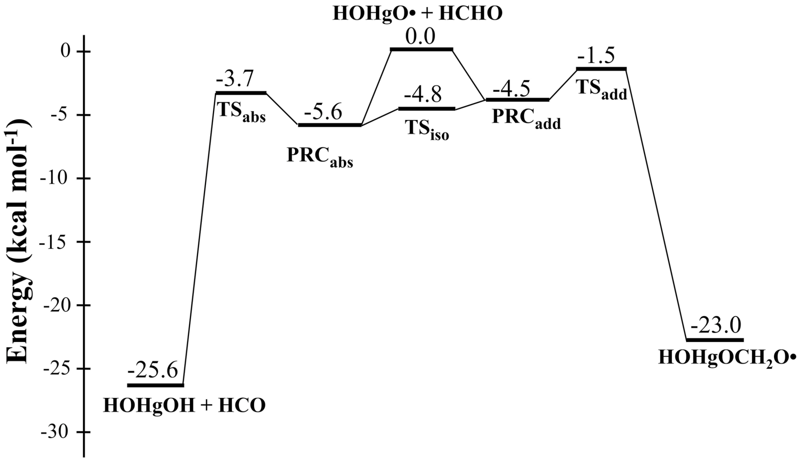

Figure 10. ZPE-corrected potential energy profile for the HOHg$^{(II)}$O$^{\bullet}$ + CH$_2$O reaction at CCSD(T)//M06-2X/AVTZ.

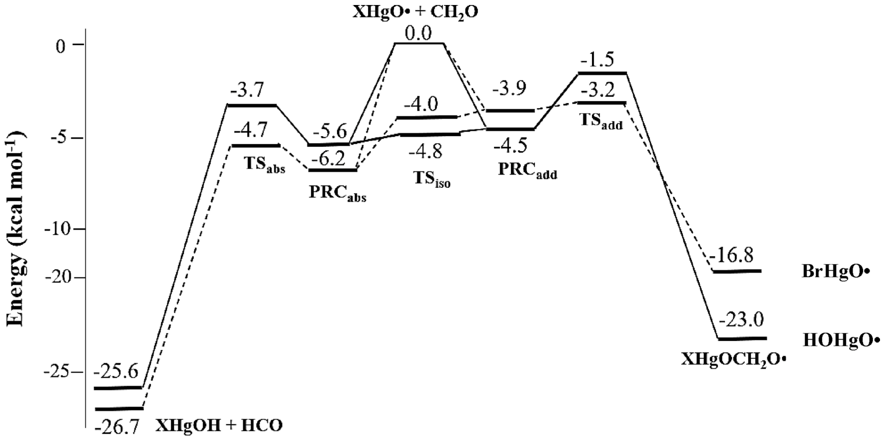

Figure 11. ZPE-corrected potential energy profiles for XHg$^{(II)}$O$^{\bullet}$ + CH$_2$O reactions at CCSD(T)//M06-2X/AVTZ. X = Br is shown with dashed lines, X = OH with solid lines.

contrasts that for OH + CH$_2$O, for which a significant energy barrier (~ 5 kcal mol^{-1}) renders the addition reaction negligible at atmospheric temperatures.[61] Figure 10 displays the PEP for the HOHg$^{(II)}$O$^{\bullet}$ + CH$_2$O system for the most stable conformers of each species.

The potential energy profile for HOHg$^{(II)}$O$^{\bullet}$ + CH$_2$O closely follows that of BrHg$^{(II)}$O$^{\bullet}$ + CH$_2$O, as is evident in Figure 11. An interesting difference is that the potential energy surface for BrHg$^{(II)}$O$^{\bullet}$ + CH$_2$O exhibits a bifurcation.[60] That is, the minimum energy path of C_{2v} symmetry branches to become two paths of C_s symmetry that each lead to a PRC and a subsequent transition state. The lack of symmetry in TS$_{\text{abstraction}}$ and PRC$_{\text{addition}}$ for HOHg$^{(II)}$O$^{\bullet}$ + CH$_2$O suggests that no such bifurcation exists here. For OH + CH$_2$O, a single PRC leads to transition states for both abstraction and addition.[61]

We find the rotational saddle point (TS$_{\text{isomerization}}$) that connects the two PRCs lies slightly below the PRC for addition in both XHg$^{(II)}$O$^{\bullet}$ + CH$_2$O systems, which is unphysical. This ordering of energies was present before correcting for zero-point energies. Presumably, M06-2X/AVTZ does not accurately describe the weak intermolecular forces controlling the structure of this transition state. We explored two structures for PRC$_{\text{addition}}$ with two different symmetries. The structure with C_1 symmetry lies ~0.5 kcal mol^{-1} below another complex with C_S symmetry. If isolated reactants form the PRC$_{\text{abstraction}}$ and PRC$_{\text{addition}}$ with comparable yields, it seems highly probable that the abstraction reaction dominates because, as shown in Figure 11:

(1) TS$_{\text{abstraction}}$ lies lower in energy than TS$_{\text{addition}}$, so formation of PRC$_{\text{abstraction}}$ is more likely to lead to reaction than is formation of PRC$_{\text{addition}}$.

(2) PRC$_{\text{abstraction}}$ lies below PRC$_{\text{addition}}$, so the conversion of PRC$_{\text{addition}}$ to PRC$_{\text{abstraction}}$ will have a higher rate constant than the reverse process.

Given the similarities in potential energy profiles for both XHg$^{(II)}$O$^{\bullet}$ + CH$_2$O systems, we also did not compute the rate constants for the HOHg$^{(II)}$O$^{\bullet}$ + CH$_2$O reaction in the current study. However, the relative energies of the saddle points for each pathway of HOHg$^{(II)}$O$^{\bullet}$ + CH$_2$O are more positive than those of the BrHg$^{(II)}$O$^{\bullet}$ + CH$_2$O system, which suggests that rate constants for HOHg$^{(II)}$O$^{\bullet}$ + CH$_2$O are smaller than those for the BrHg$^{(II)}$O$^{\bullet}$ + CH$_2$O system. In terms of the ratio $k_{\text{abstraction}}/k_{\text{addition}}$, considering the similarities in potential energy surfaces, we suggest that the ratio $k_{\text{abstraction}}/k_{\text{addition}}$ for the HOHg$^{(II)}$O$^{\bullet}$ + CH$_2$O system would approximate the 10:1 value calculated for BrHg$^{(II)}$O$^{\bullet}$ + CH$_2$O.

3.5. HOHg$^{(II)}$O$^{\bullet}$ + CO → HOHg$^{(I)\bullet}$ + CO$_2$. The reaction HOHg$^{(II)}$O$^{\bullet}$ + CO → HOHg$^{(I)\bullet}$ + CO$_2$ follows the same mechanism as Khiri et al.,[62] found for BrHg$^{(II)}$O$^{\bullet}$ + CO. HOHg$^{(II)}$O$^{\bullet}$ can interact with CO to form two isomeric van der Waals complexes. The less stable HOHg$^{(II)}$O$^{\bullet}$--OC complex

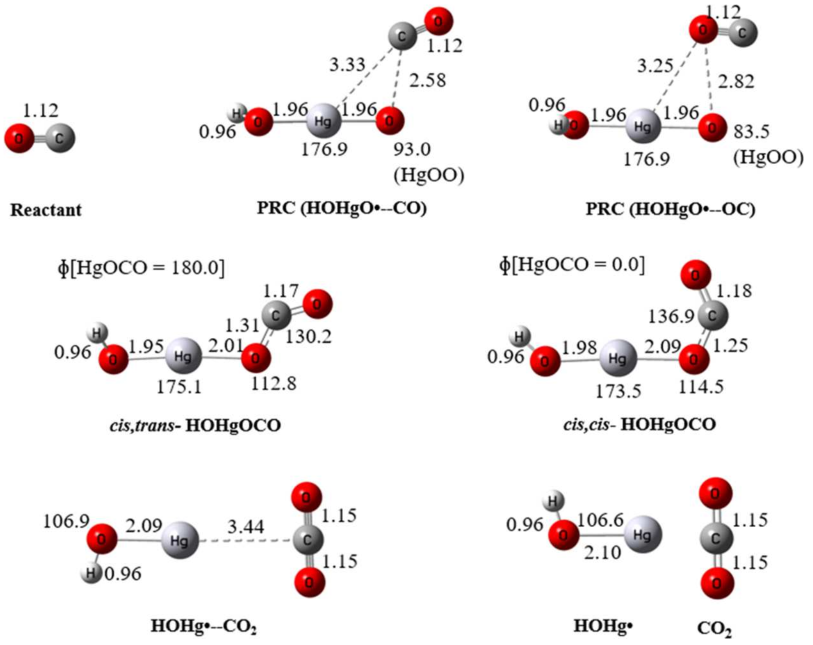

Figure 12. Geometries of all minima for the reaction $HOHg^{(II)}O^{\bullet}$ + CO (distances in Å, bond angles and dihedral angles in degrees) optimized at M06-2X/AVTZ. All species with more than three atoms belong to the C_1 point group, except the $HOHg^{(I)\bullet}$--CO_2 complex (C_s).

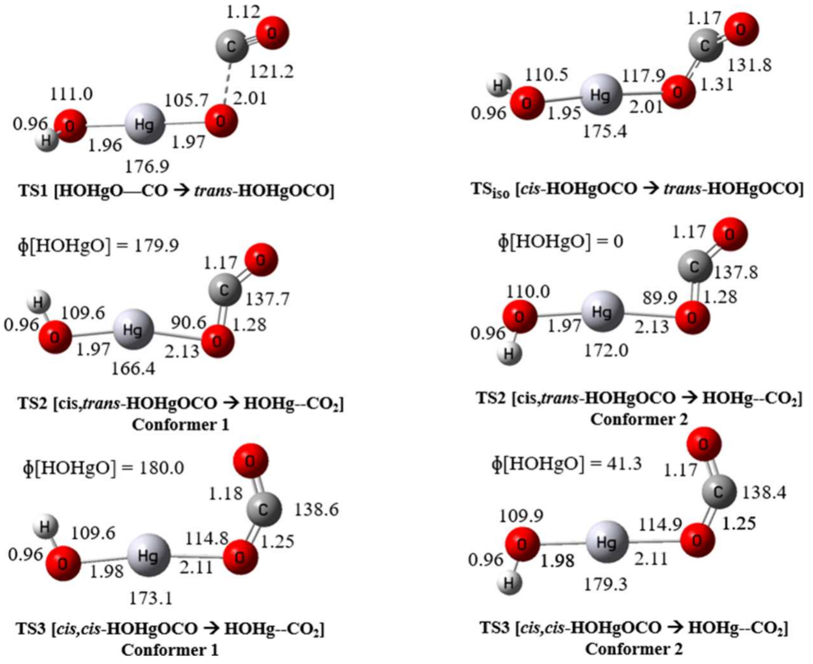

Figure 13. Geometries of all transition states (distances in Å, bond angles and dihedral angles in degrees) optimized at M06-2X/AVTZ. Conformer 1 of TS2 and TS3 has C_s symmetry, while all other saddle points belong to the C_1 point group.

does not appear to be involved in the overall reaction. The complex $HOHg^{(II)}O^{\bullet}$--CO constitutes the PRC for the overall reaction. This PRC can react via a submerged energy barrier (TS1) to form $HOHg^{(II)}OCO$. The initially formed conformer has the hydroxyl hydrogen cis to the C=O moiety and ϕ(HgOCO) of 180°, and we label it *cis,trans* (note that neither conformer is actually planar). This conformer can isomerize over a rotational saddle point (TS_{iso}) to the *cis,cis* conformer. Figure 12 depicts geometries of potential energy minima, and Figure 13 shows the structures of transition states. Both isomers of $HOHg^{(II)}OCO$ can easily reorganize to produce a $HOHg^{(I)\bullet}$--CO_2 complex that will rapidly dissociate to $HOHg^{(I)\bullet}$ + CO_2. Each conformer of $HOHg^{(II)}OCO$ possesses two TSs for dissociation to $HOHg^{(I)\bullet}$--CO_2, as shown in Figure 13. Figure 14 shows the potential energy profile of the overall reaction.

As seen from Figure 14, $HOHg^{(II)}O^{\bullet}$ + CO and $BrHg^{(II)}O^{\bullet}$ + CO share very similar potential energy profiles. For both reactions, the more stable entrance channel complex ($XHg^{(II)}O^{\bullet}$--CO) is the prereactive complex. The barrier from $XHg^{(II)}O^{\bullet}$--CO to *trans*-$XHg^{(II)}OCO$ (TS1) lies submerged by 1.2 kcal mol^{-1} ($HOHg^{(II)}OCO$) or 1.5 kcal mol^{-1} ($BrHg^{(II)}OCO$) with respect to the separated reactants. If this

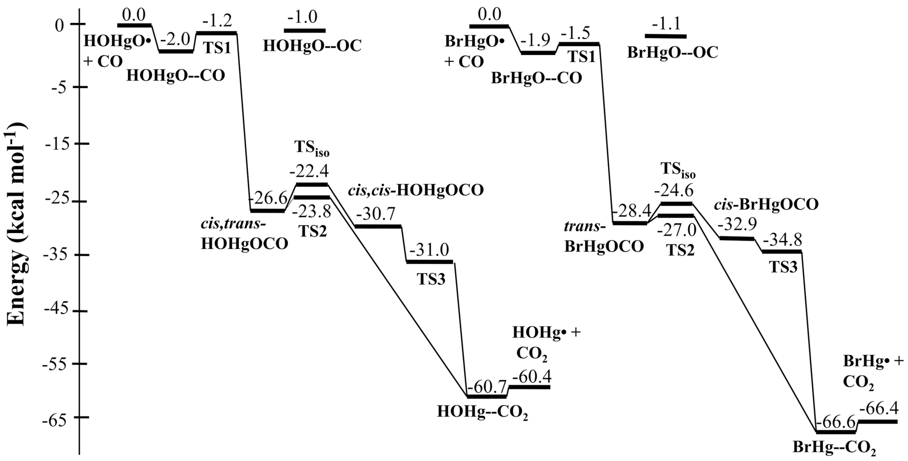

Figure 14. Potential energy profiles for $HOHg^{(II)}O\bullet$ + CO and $BrHg^{(II)}O^{\bullet}$ + CO[62] at CCSD(T)//M06-2X/AVTZ and CCSD(T)/CBS + ΔCV + ΔPP + ΔSO level of theories respectively. Relative energies are corrected for zero-point energies.

difference is real rather than an artifact of different model chemistries, it would tend to make $k(HOHg^{(II)}O^{\bullet} + CO)$ smaller than $k(BrHg^{(II)}O^{\bullet} + CO)$. The two conformers of $XHg^{(II)}OCO$ are linked by a rotational saddle point (labeled as TS_{iso}) and lie well below separated reactants (26−33 kcal mol^{-1}), making the back reaction unlikely. The barrier for *trans*-$XHg^{(II)}OCO$ dissociating to $XHg^{(I)\bullet}$--CO_2 complex (TS2) is quite small (~1−3 kcal mol^{-1}), so that chemically activated $XHg^{(II)}OCO$ will promptly dissociate to $XHg^{(I)\bullet}$ + CO_2.[62] There was no energy barrier going from *cis,cis*-$HOHg^{(II)}OCO$ to $HOHg^{(I)\bullet}$--CO_2 as the transition state connecting the two minima was submerged by 0.3 kcal mol^{-1} with respect to the former. Readers wishing to compare these systems to the potential energy profile for OH + CO are directed to the references cited here.[63,64]

Khiri et al.[62] speculated that energy deposited in $BrHg^{(I)\bullet}$ produced from $BrHg^{(II)}O^{\bullet}$ + CO might enable prompt dissociation of $BrHg^{(I)\bullet}$. In the analogous reaction studied here, we note that in $HOHg^{(II)}OCO$ itself, the O−C−O angles are very nonlinear and the HgO-C═O distance is much longer than in CO_2. This suggests that much of the vibrational energy in the products will be in the OCO bend and CO stretch. By contrast, the $HOHg^{(I)\bullet}$ moiety has nearly the same bond angle and HO distance as in the isolated HOHg radical. The O−Hg distance does increase significantly upon forming $HOHg^{(I)}\bullet$ (from 1.96 to 2.10 Å), which might lead one to expect $HOHg^{(I)\bullet}$ to be formed with significant vibrational energy. However, the $HO{-}Hg^{\bullet}$ vibrational frequency of ~400 cm^{-1} corresponds to a force constant of only 141 kg s^2. This means that compressing $HOHg^{(I)\bullet}$ from 2.10 to 1.96 Å without accessing the classically forbidden region is already possible at v = 2 (in the harmonic oscillator approximation). Two quanta of 400 cm^{-1} constitute only 20% of the 3850 cm^{-1} (11.0 kcal mol^{-1}) bond energy of $HOHg^{(I)\bullet}$.[49] Consequently, we think it unlikely that $HOHg^{(I)\bullet}$ produced in this reaction will promptly dissociate.

4. ATMOSPHERIC IMPLICATIONS

The reactions of $HOHg^{(II)}O^{\bullet}$ with NO and NO_2 could be significant in determining the fate of $HOHg^{(II)}O^{\bullet}$ in the continental boundary layer, given the high reaction rate constants and relatively high concentrations of NO_x. By analogy to $BrHg^{(II)}ONO$,[38] we expect $HOHg^{(II)}ONO$ produced from $HOHg^{(II)}O^{\bullet}$ + NO to photolyze fairly rapidly by $HOHg^{(II)}O$-NO bond dissociation. Hence, the reaction with NO does little to determine the fate of $HOHg^{(II)}O^{\bullet}$. The reaction $HOHg^{(II)}O^{\bullet}$ + NO_2 likely plays a larger role due to the formation of thermally stable $HOHg^{(II)}ONO_2$. $HOHg^{(II)}ONO_2$ would most likely undergo dry or wet deposition or, potentially, photolysis.

$HOHg^{(II)}O^{\bullet}$ reacts with CH_4 by abstracting an H atom to form $Hg^{(II)}(OH)_2$, and this behavior will extend to abstracting hydrogen from sp^3-hybridized carbon atoms of other volatile organic compounds. We suggest that the rate constants for these reactions are larger than that for $HOHg^{(II)}O^{\bullet}$ + CH_4, just as this is true for OH.[65,66] The fate of $Hg^{(II)}(OH)_2$ is suggested to be wet and dry deposition or photolysis. However, currently, we do not have the data required to estimate the photolysis rate constant for $Hg^{(II)}(OH)_2$. Stromberg et al.[58] reported the low-lying excitation of $Hg^{(II)}(OH)_2$ molecule to have a vertical excitation energy of 6.3 eV, suggesting λ_{max} of 197 nm. But they did not calculate absorption cross sections versus wavelength, so we do not know if this transition extends to wavelengths reaching the troposphere ($\lambda \geq 300$ nm).

$HOHg^{(II)}O^{\bullet}$ adds to C_2H_4 exothermically through a submerged barrier, and we expect the same reaction mechanism to hold in reactions with larger alkenes. By analogy to OH + alkenes, we anticipate the rate constant to be higher for larger alkenes than for ethylene.[65,66] We assume that the $HOHg^{(II)}OCH_2CH_2^{\bullet}$ product of the $HOHg^{(II)}O^{\bullet}$ + C_2H_4 system reacts like any carbon-centered radical; that is, it adds O_2 to form $HOHg^{(II)}OCH_2CH_2OO^{\bullet}$, which might then react with HOO or NO.

The reaction $HOHg^{(II)}O^{\bullet}$ + CH_2O will mostly produce $Hg^{(II)}(OH)_2$ via H-atom abstraction rather than undergo addition to form $HOHg^{(II)}OCH_2O^{\bullet}$. Larger aldehydes tend to have larger RC(═O)-H bond energies than CH_2O,[53] so the preference for addition may not hold for larger aldehydes. We have not investigated $HOHg^{(II)}O^{\bullet}$ addition to ketones (RC(═O)R') or larger aldehydes to produce $HOHg^{(II)}OCRR'O^{\bullet}$. These reactions, along with $HOHg^{(II)}O\bullet$ + alkenes, lead to organic mercury compounds, which are generally believed to pose greater health risks than inorganic mercury.[67]

Unlike the reactions discussed above, $HOHg^{(II)}O\bullet$ + CO leads to the reduction of $Hg^{(II)}$ into $Hg^{(I)}$. The $HOHg^{(I)}\bullet$ formed from this reaction may dissociate back to $Hg^{(0)}$ + OH, either thermally or (although we think it unlikely) via chemical activation. Hence, the competition between $HOHg^{(II)}O\bullet$ + CO

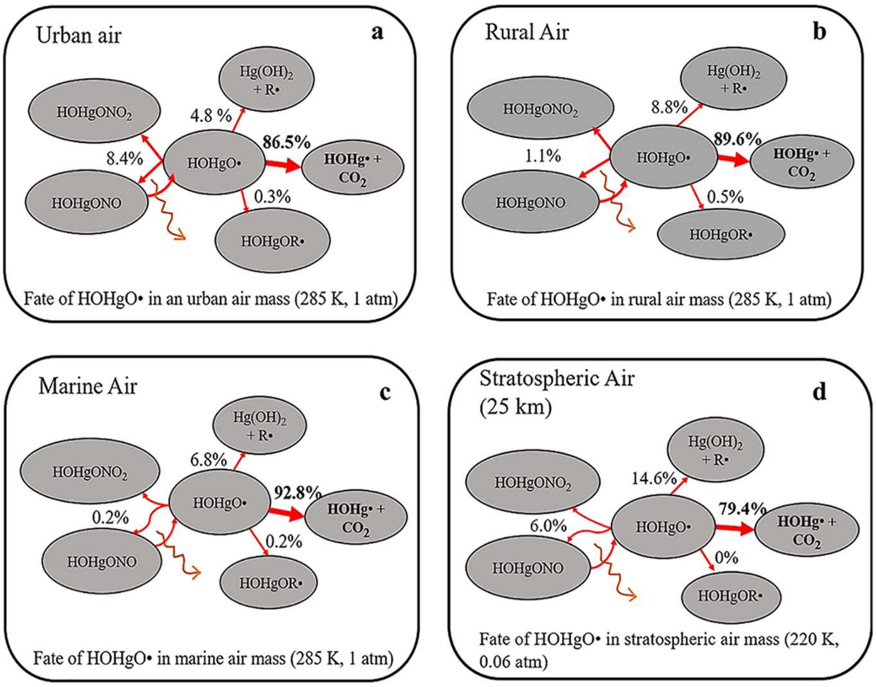

Figure 15. Predicted fates of $HOHg^{(II)}O^\bullet$ in four air masses at the ground level (a- urban air; b- rural air; c- marine air; and d- stratospheric air).

and $HOHg^{(II)}O\bullet$ reactions forming stable $Hg^{(II)}$ compounds could greatly affect the burden of $Hg^{(II)}$ in the atmosphere.

Finally, we assessed the fate of $HOHg^{(II)}O^\bullet$ under various atmospheric conditions, while taking all six reactions into account. We calculated the fraction of $HOHg^{(II)}O^\bullet$ reacted with each trace gas, A, by computing their pseudo-first order rate constants $k'_A = k_A[A]$ where k_A is the bimolecular rate constant for $HOHg^{(II)}O^\bullet$ reacting with trace gas A. Rate constants were assumed to equal those adopted for $BrHg^{(II)}O^\bullet + A$ computed at CCSD(T)//M06-2X/AVTZ[38,60] (see Table S12) with two exceptions. For $HOHg^{(II)}O^\bullet + CH_4$, we used the rate constants calculated here. For $HOHg^{(II)}O^\bullet$ + CO, we take the value assumed by Shah et al. (2021)[28] in the latest GEOS-Chem simulations. We considered compositions representative of four air masses: ground level air in urban, rural, and marine environments, plus stratospheric air. Table S12 lists the concentration values and data sources. Figure 15 displays the calculated fate of $HOHg^{(II)}O\bullet$ at four different air masses.

Based on previous results for $BrHg^{(II)}O^\bullet$, we expected that CH_4 and CO would compete to largely determine the fate of $HOHg^{(II)}O^\bullet$. Instead, we find that the reaction with CO dominates (79−93%) in all four air masses. The lesser role for reaction with CH_4 here (<15%) arises from the lower rate constant for $HOHg^{(II)}O^\bullet + CH_4$ versus $BrHg^{(II)}O^\bullet + CH_4$. In urban air, where $[NO_x]$ is high, NO_x (8%) can outcompete methane (5%). The addition reactions of $HOHg^{(II)}O^\bullet$ with C_2H_4 and CH_2O contribute 0.5% or less in all four air masses. The accuracy of these estimates is largely limited by two major factors. The first is that better rate constants are needed for $HOHg^{(II)}O^\bullet$ reactions with CH_4 and CO to more reliably determine whether $HOHg^{(II)}O^\bullet$ is reduced to $Hg^{(I)}$ or forms closed-shell $Hg^{(II)}$ compounds. Second, we only considered a few reactions of $HOHg^{(II)}O^\bullet$, whereas $HOHg^{(II)}O^\bullet$ could react with a myriad of VOCs, and possibly with ozone.[30] To improve the reliability of modeling of regional and global mercury, our group is working on improving rate constants for reactions of $XHg^{(II)}O^\bullet$ with methane and CO and determining rate constants for $XHg^{(II)}O^\bullet + O_3$.

■ ASSOCIATED CONTENT

SI Supporting Information

The Supporting Information is available free of charge at https://pubs.acs.org/doi/10.1021/acs.jpca.3c04159.

> Absolute energies, ZPEs, Cartesian coordinates, vibrational frequencies, rotational constants, and T_1 diagnostics for all species; enthalpy changes and critical energies for each reaction; Gibbs free energies as a function of temperature along the MEP for $HOHg^{(II)}O^\bullet + CH_4$; temperature dependent effective rate constants for $HOHg^{(II)}O^\bullet + CH_4$; atmospheric concentrations and rate constants for predicting the fate of $HOHg^{(II)}O^\bullet$ (PDF)

■ AUTHOR INFORMATION

Corresponding Author

Theodore S. Dibble − *Department of Chemistry, State University of New York, College of Environmental Science and Forestry, Syracuse, New York 13210, United States;* orcid.org/0000-0002-0023-8233; Phone: (315) 470-6596; Email: tsdibble@esf.edu

Authors

Darshi T. Hewa Edirappulige − *Department of Chemistry, State University of New York, College of Environmental Science and Forestry, Syracuse, New York 13210, United States*

Ilena J. Kirby − *Department of Chemistry, State University of New York, College of Environmental Science and Forestry, Syracuse, New York 13210, United States*

Camille K. Beckett − *Department of Chemistry, State University of New York, College of Environmental Science and Forestry, Syracuse, New York 13210, United States*

Complete contact information is available at:
https://pubs.acs.org/10.1021/acs.jpca.3c04159

Notes

The authors declare no competing financial interest.

■ ACKNOWLEDGMENTS

This material is based upon work supported by the National Science Foundation under Grants 1609848 and 2004100. We thank Pedro J. Castro for providing guidance on calculations.

■ REFERENCES

(1) Zhang, L.; Wang, S.; Wu, Q.; Wang, F.; Lin, C.-J.; Zhang, L.; Hui, M.; Yang, M.; Su, H.; Hao, J. Mercury Transformation and Speciation in Flue Gases from Anthropogenic Emission Sources: A Critical Review. *Atmos. Chem. Phys.* **2016**, *16* (4), 2417−2433.

(2) Driscoll, C. T.; Mason, R. P.; Chan, H. M.; Jacob, D. J.; Pirrone, N. Mercury as a Global Pollutant: Sources, Pathways, and Effects. *Environ. Sci. Technol.* **2013**, *47* (10), 4967−4983.

(3) Lin, C.-J.; Pehkonen, S. O. The Chemistry of Atmospheric Mercury: A Review. *Atmos. Environ.* **1999**, *33* (13), 2067−2079.

(4) Pirrone, N.; Mahaffey, K. R. Where We Stand on Mercury Pollution and Its Health Effects on Regional and Global Scales. In *Dynamics of Mercury Pollution on Regional and Global Scales: Atmospheric Processes and Human Exposures Around the World*; Pirrone, N.; Mahaffey, K. R., Eds.; Springer US: Boston, MA, 2005; pp 1−21. DOI: 10.1007/0-387-24494-8_1.

(5) Jiskra, M.; Sonke, J. E.; Obrist, D.; Bieser, J.; Ebinghaus, R.; Myhre, C. L.; Pfaffhuber, K. A.; Wängberg, I.; Kyllönen, K.; Worthy, D. E. J.; et al. A Vegetation Control on Seasonal Variations in Global Atmospheric Mercury Concentrations. *Nat. Geosci.* **2018**, *11*, 244−250.

(6) Zhou, J.; Obrist, D.; Dastoor, A.; Jiskra, M.; Ryjkov, A. Vegetation Uptake of Mercury and Impacts on Global Cycling. *Nat. Rev. Earth Environ.* **2021**, *2*, 269−284.

(7) Schroeder, W. H.; Munthe, J. Atmospheric Mercury—An Overview. *Atmos. Environ.* **1998**, *32*, 809−822.

(8) Lin, C.-J.; Pongprueksa, P.; Bullock, O. R.; Lindberg, S. E.; Pehkonen, S. O.; Jang, C.; Braverman, T.; Ho, T. C. Scientific Uncertainties in Atmospheric Mercury Models II: Sensitivity Analysis in the CONUS Domain. *Atmos. Environ.* **2007**, *41* (31), 6544−6560.

(9) Bullock, O. R.; Brehme, K. A. Atmospheric Mercury Simulation Using the CMAQ Model: Formulation Description and Analysis of Wet Deposition Results. *Atmos. Environ.* **2002**, *36* (13), 2135−2146.

(10) Bieser, J.; De Simone, F.; Gencarelli, C.; Geyer, B.; Hedgecock, I.; Matthias, V.; Travnikov, O.; Weigelt, A. A Diagnostic Evaluation of Modeled Mercury Wet Depositions in Europe Using Atmospheric Speciated High-Resolution Observations. *Environ. Sci. Pollut. Res.* **2014**, *21* (16), 9995−10012.

(11) De Simone, F.; Gencarelli, C. N.; Hedgecock, I. M.; Pirrone, N. Global Atmospheric Cycle of Mercury: A Model Study on the Impact of Oxidation Mechanisms. *Environ. Sci. Pollut. Res. Int.* **2014**, *21* (6), 4110−4123.

(12) Gencarelli, C. N.; Bieser, J.; Carbone, F.; De Simone, F.; Hedgecock, I. M.; Matthias, V.; Travnikov, O.; Yang, X.; Pirrone, N. Sensitivity Model Study of Regional Mercury Dispersion in the Atmosphere. *Atmos. Chem. Phys.* **2017**, *17* (1), 627−643.

(13) Pal, B.; Ariya, P. A. Studies of Ozone Initiated Reactions of Gaseous Mercury: Kinetics, Product Studies, and Atmospheric Implications. *Phys. Chem. Chem. Phys.* **2004**, *6* (3), 572−579.

(14) Snider, G.; Raofie, F.; Ariya, P. A. Effects of Relative Humidity and CO(g) on the O_3-Initiated Oxidation Reaction of Hg^0(g): Kinetic & Product Studies. *Phys. Chem. Chem. Phys.* **2008**, *10* (36), 5616.

(15) Shepler, B. C.; Peterson, K. A. Mercury Monoxide: A Systematic Investigation of Its Ground Electronic State. *J. Phys. Chem. A* **2003**, *107* (11), 1783−1787.

(16) Saiz-Lopez, A.; Acuña, A. U.; Mahajan, A. S.; Dávalos, J. Z.; Feng, W.; Roca-Sanjuán, D.; Carmona-García, J.; Cuevas, C. A.; Kinnison, D. E.; Gómez Martín, J. C. The Chemistry of Mercury in the Stratosphere. *Geophys. Res. Lett.* **2022**, *49* (12), No. e2022GL097953.

(17) Holmes, C. D.; Jacob, D. J.; Yang, X. Global Lifetime of Elemental Mercury against Oxidation by Atomic Bromine in the Free Troposphere. *Geophys. Res. Lett.* **2006**, *33*, L20808.

(18) Dibble, T. S.; Zelie, M. J.; Mao, H. Thermodynamics of Reactions of ClHg and BrHg Radicals with Atmospherically Abundant Free Radicals. *Atmospheric Chem. Phys.* **2012**, *12* (21), 10271−10279.

(19) Holmes, C. D.; Jacob, D. J.; Mason, R. P.; Jaffe, D. A. Sources and Deposition of Reactive Gaseous Mercury in the Marine Atmosphere. *Atmos. Environ.* **2009**, *43* (14), 2278−2285.

(20) Wang, S.; Schmidt, J. A.; Baidar, S.; Coburn, S.; Dix, B.; Koenig, T. K.; Apel, E.; Bowdalo, D.; Campos, T. L.; Eloranta, E.; et al. Active and Widespread Halogen Chemistry in the Tropical and Subtropical Free Troposphere. *Proc. Natl. Acad. Sci. U. S. A.* **2015**, *112* (30), 9281−9286.

(21) Ye, Z.; Mao, H.; Lin, C.-J.; Kim, S. Y. Investigation of Processes Controlling Summertime Gaseous Elemental Mercury Oxidation at Midlatitudinal Marine, Coastal, and Inland Sites. *Atmos. Chem. Phys.* **2016**, *16* (13), 8461−8478.

(22) Steffen, A.; Douglas, T.; Amyot, M.; Ariya, P.; Aspmo, K.; Berg, T.; Bottenheim, J.; Brooks, S.; Cobbett, F.; Dastoor, A.; et al. A Synthesis of Atmospheric Mercury Depletion Event Chemistry in the Atmosphere and Snow. *Atmos. Chem. Phys.* **2008**, *8* (6), 1445−1482.

(23) Custard, K. D.; Thompson, C. R.; Pratt, K. A.; Shepson, P. B.; Liao, J.; Huey, L. G.; Orlando, J. J.; Weinheimer, A. J.; Apel, E.; Hall, S. R.; et al. The NOx Dependence of Bromine Chemistry in the Arctic Atmospheric Boundary Layer. *Atmos. Chem. Phys.* **2015**, *15* (18), 10799−10809.

(24) Wang, S.; Pratt, K. A. Molecular Halogens Above the Arctic Snowpack: Emissions, Diurnal Variations, and Recycling Mechanisms. *J. Geophys. Res. Atmos.* **2017**, *122* (21), 11,991−12,007.

(25) Gabay, M.; Raveh-Rubin, S.; Peleg, M.; Fredj, E.; Tas, E. Is Oxidation of Atmospheric Mercury Controlled by Different Mechanisms in the Polluted Continental Boundary Layer vs. Remote Marine Boundary Layer? *Environ. Res. Lett.* **2020**, *15* (6), No. 064026.

(26) Holmes, C. D.; Jacob, D. J.; Corbitt, E. S.; Mao, J.; Yang, X.; Talbot, R.; Slemr, F. Global Atmospheric Model for Mercury Including Oxidation by Bromine Atoms. *Atmos. Chem. Phys.* **2010**, *10* (24), 12037−12057.

(27) Travnikov, O.; Angot, H.; Artaxo, P.; Bencardino, M.; Bieser, J.; D'Amore, F.; Dastoor, A.; De Simone, F.; Diéguez, M. D. C.; Dommergue, A.; et al. Multi-Model Study of Mercury Dispersion in the Atmosphere: Atmospheric Processes and Model Evaluation. *Atmos. Chem. Phys.* **2017**, *17* (8), 5271−5295.

(28) Shah, V.; Jacob, D. J.; Thackray, C. P.; Wang, X.; Sunderland, E. M.; Dibble, T. S.; Saiz-Lopez, A.; Černušák, I.; Kellö, V.; Castro, P. J.; et al. Improved Mechanistic Model of the Atmospheric Redox Chemistry of Mercury. *Environ. Sci. Technol.* **2021**, *55* (21), 14445−14456.

(29) Saiz-Lopez, A.; Travnikov, O.; Sonke, J. E.; Thackray, C. P.; Jacob, D. J.; Carmona-García, J.; Francés-Monerris, A.; Roca-Sanjuán, D.; Acuña, A. U.; Dávalos, J. Z.; et al. Photochemistry of Oxidized Hg(I) and Hg(II) Species Suggests Missing Mercury Oxidation in the Troposphere. *Proc. Natl. Acad. Sci. U. S. A.* **2020**, *117* (49), 30949−30956.

(30) Gómez Martín, J. C.; Lewis, T. R.; Douglas, K. M.; Blitz, M. A.; Saiz-Lopez, A.; Plane, J. M. C. The Reaction between HgBr and O_3: Kinetic Study and Atmospheric Implications. *Phys. Chem. Chem. Phys.* **2022**, *24* (20), 12419−12432.

(31) Castro, P. J.; Kellö, V.; Cernušák, I.; Dibble, T. S. Together, Not Separately, OH and O3 Oxidize Hg(0) to Hg(II) in the Atmosphere. *J. Phys. Chem. A* **2022**, *126* (44), 8266−8279.

(32) Balabanov, N. B.; Peterson, K. A. Mercury and Reactive Halogens: The Thermochemistry of Hg + {Cl_2, Br_2, BrCl, ClO, and BrO}. *J. Phys. Chem. A* **2003**, *107* (38), 7465−7470.

(33) Frisch, M. J.; Trucks, G. W.; Schlegel, H. B.; Scuseria, G. E.; Robb, M. A.; Cheeseman, J. R.; Scalmani, G.; Barone, V.; Petersson, G.

A.; Nakatsuji, H. et al. *Gaussian 16 Rev. C.01*; Gaussian, Inc.: Wallingford, CT, 2016.

(34) Montero-Campillo, M. M.; Lamsabhi, A. M.; Mó, O.; Yáñez, M. Alkyl Mercury Compounds: An Assessment of DFT Methods. *Theor. Chem. Acc.* **2013**, *132* (3), 1328.

(35) Jiao, Y.; Dibble, T. S. First Kinetic Study of the Atmospherically Important Reactions $\mathrm{BrH\dot{g}}$ + NO_2 and $\mathrm{BrH\dot{g}}$ + HOO. *Phys. Chem. Chem. Phys.* **2017**, *19* (3), 1826−1838.

(36) Jiao, Y.; Dibble, T. S. Quality Structures, Vibrational Frequencies, and Thermochemistry of the Products of Reaction of $BrHg^{\bullet}$ with NO_2, HO_2, ClO, BrO, and IO. *J. Phys. Chem. A* **2015**, *119* (42), 10502−10510.

(37) Jiao, Y.; Dibble, T. S. Structures, Vibrational Frequencies, and Bond Energies of the BrHgOX and BrHgXO Species Formed in Atmospheric Mercury Depletion Events. *J. Phys. Chem. A* **2017**, *121* (41), 7976−7985.

(38) Lam, K. T.; Wilhelmsen, C. J.; Schwid, A. C.; Jiao, Y.; Dibble, T. S. Computational Study on the Photolysis of BrHgONO and the Reactions of $BrHgO^{\bullet}$ with CH_4, C_2H_6, NO, and NO_2: Implications for Formation of Hg(II) Compounds in the Atmosphere. *J. Phys. Chem. A* **2019**, *123* (8), 1637−1647.

(39) Zhao, Y.; Truhlar, D. G. The M06 Suite of Density Functionals for Main Group Thermochemistry, Thermochemical Kinetics, Noncovalent Interactions, Excited States, and Transition Elements: Two New Functionals and Systematic Testing of Four M06-Class Functionals and 12 Other Functionals. *Theor. Chem. Acc.* **2008**, *120* (1), 215−241.

(40) Dunning, T. H., Jr.; Hay, P. J. Gaussian Basis Sets for Molecular Calculations. In *Methods of Electronic Structure Theory*; Schaefer, H. F. Ed.; Springer US: Boston, MA, 1977; pp 1−27. DOI: 10.1007/978-1-4757-0887-5_1.

(41) Kendall, R. A.; Dunning, T. H., Jr.; Harrison, R. J. Electron Affinities of the First-Row Atoms Revisited. Systematic Basis Sets and Wave Functions. *J. Chem. Phys.* **1992**, *96* (9), 6796−6806.

(42) Balabanov, N. B.; Peterson, K. A. Systematically Convergent Basis Sets for Transition Metals. I. All-Electron Correlation Consistent Basis Sets for the 3d Elements Sc-Zn. *J. Chem. Phys.* **2005**, *123* (6), 64107.

(43) Figgen, D.; Rauhut, G.; Dolg, M.; Stoll, H. Energy-Consistent Pseudopotentials for Group 11 and 12 Atoms: Adjustment to Multi-Configuration Dirac−Hartree−Fock Data. *Chem. Phys.* **2005**, *311* (1), 227−244.

(44) Peterson, K. A. Systematically Convergent Basis Sets with Relativistic Pseudopotentials. I. Correlation Consistent Basis Sets for the Post-d Group 13−15 Elements. *J. Chem. Phys.* **2003**, *119*, 11099−11112.

(45) Raghavachari, K.; Trucks, G. W.; Pople, J. A.; Head-Gordon, M. A Fifth-Order Perturbation Comparison of Electron Correlation Theories. *Chem. Phys. Lett.* **1989**, *157* (6), 479−483.

(46) Forst, W. *Unimolecular Reactions: A Concise Introduction*; Cambridge University Press, 2003; pp 189−194.

(47) Yang, L.; Sonk, J. A.; Barker, J. R. HO + OClO Reaction System: Featuring a Barrierless Entrance Channel with Two Transition States. *J. Phys. Chem. A* **2015**, *119* (22), 5723−5731.

(48) Espinosa-García, J.; Valle, F. J. O.; del Corchado, J. C. Transition State Theory and Eckart's Tunnelling Factor: A Good Approximation for the Calculation of Bimolecular Rate Constants? *Chem. Phys.* **1994**, *183* (1), 95−100.

(49) Dibble, T. S.; Tetu, H. L.; Jiao, Y.; Thackray, C. P.; Jacob, D. J. Modeling the OH-Initiated Oxidation of Mercury in the Global Atmosphere without Violating Physical Laws. *J. Phys. Chem. A* **2020**, *124* (2), 444−453.

(50) Golden, D. M.; Barker, J. R.; Lohr, L. L. Master Equation Models for the Pressure- and Temperature-Dependent Reactions HO + NO_2 → $HONO_2$ and HO + NO_2 → HOONO. *J. Phys. Chem. A* **2003**, *107* (50), 11057−11071.

(51) Fry, J. L.; Nizkorodov, S. A.; Okumura, M.; Roehl, C. M.; Francisco, J. S.; Wennberg, P. O. Cis-Cis and Trans-Perp HOONO: Action Spectroscopy and Isomerization Kinetics. *J. Chem. Phys.* **2004**, *121* (3), 1432−1448.

(52) Papayannis, D. K.; Kosmas, A. M. The Conformational Potential Energy Surface of IOONO and the Isomerization and Decomposition Processes. *Chem. Phys.* **2005**, *315* (3), 251−258.

(53) Burkholder, J. B.; Sander, S. P.; Abbatt, J.; Barker, J. R.; Cappa, C.; Crounse, J. D.; Dibble, T. S.; Huie, R. E.; Kolb, C. E.; Kurylo, M. J.; Orkin, V. L. et al.*Chemical Kinetics and Photochemical Data for Use in Atmospheric Studies, Evaluation No. 19*; Jet Propulsion Laboratory, National Aeronautics and Space Administration: Pasadena, 2019; https://jpldataeval.jpl.nasa.gov/.

(54) Kovačič, S.; Lesar, A.; Hodoščcek, M.; Koller, J. A Theoretical Examination of the Isomerization of $BrONO_2$ to BrOONO. *Chem. Phys.* **2006**, *323* (2), 369−375.

(55) Dibble, T. S.; Francisco, J. S. Structure, Vibrational Frequencies, and Stability of a Reactive Intermediate: FOONO. *J. Am. Chem. Soc.* **1997**, *119* (12), 2894−2895.

(56) Ellingson, B. A.; Pu, J.; Lin, H.; Zhao, Y.; Truhlar, D. G. Multicoefficient Gaussian-3 Calculation of the Rate Constant for the OH + CH_4 Reaction and Its $^{12}C/^{13}C$ Kinetic Isotope Effect with Emphasis on the Effects of Coordinate System and Torsional Treatment. *J. Phys. Chem. A* **2007**, *111* (45), 11706−11717.

(57) Francés-Monerris, A.; Carmona-García, J.; Acuña, A. U.; Dávalos, J. Z.; Cuevas, C. A.; Kinnison, D. E.; Francisco, J. S.; Saiz-Lopez, A.; Roca-Sanjuán, D. Photodissociation Mechanisms of Major Mercury(II) Species in the Atmospheric Chemical Cycle of Mercury. *Angew. Chem., Int. Ed. Engl.* **2020**, *59* (19), 7605−7610.

(58) Strömberg, D.; Gropen, O.; Wahlgren, U. Non-Relativistic and Relativistic Calculations on Some Zn, Cd and Hg Complexes. *Chem. Phys.* **1989**, *133* (2), 207−219.

(59) Wang, X.; Andrews, L. Infrared Spectrum of $Hg(OH)_2$ in Solid Neon and Argon. *Inorg. Chem.* **2005**, *44* (1), 108−113.

(60) Lam, K. T.; Wilhelmsen, C. J.; Dibble, T. S. $BrHgO^{\bullet}$ + C_2H_4 and $BrHgO^{\bullet}$ + HCHO in Atmospheric Oxidation of Mercury: Determining Rate Constants of Reactions with Prereactive Complexes and Bifurcation. *J. Phys. Chem. A* **2019**, *123* (28), 6045−6055.

(61) Akbar Ali, M.; Barker, J. R. Comparison of Three Isoelectronic Multiple-Well Reaction Systems: OH + CH_2O, OH + CH_2CH_2, and OH + CH_2NH. *J. Phys. Chem. A* **2015**, *119* (28), 7578−7592.

(62) Khiri, D.; Louis, F.; Černušák, I.; Dibble, T. S. $BrHgO^{\bullet}$ + CO: Analogue of OH + CO and Reduction Path for Hg(II) in the Atmosphere. *ACS Earth Space Chem.* **2020**, *4* (10), 1777−1784.

(63) Tajti, A.; Szalay, P. G.; Császár, A. G.; Kállay, M.; Gauss, J.; Valeev, E. F.; Flowers, B. A.; Vázquez, J.; Stanton, J. F. HEAT: High Accuracy Extrapolated Ab Initio Thermochemistry. *J. Chem. Phys.* **2004**, *121* (23), 11599−11613.

(64) Nguyen, T. L.; Xue, B. C.; Weston, R. E.; Barker, J. R.; Stanton, J. F. Reaction of HO with CO: Tunneling Is Indeed Important. *J. Phys. Chem. Lett.* **2012**, *3* (11), 1549−1553.

(65) McGillen, M. R.; Carter, W. P. L.; Mellouki, W.; Orlando, J. J.; Picquet-Varrault, B.; Wallington, T. J. Database for the Kinetics of the Gas-Phase Atmospheric Reactions of Organic Compounds. https://doi.org/10.25326/36/, (accessed March 21, 2023).

(66) McGillen, M. R.; Carter, W. P. L.; Mellouki, A.; Orlando, J. J.; Picquet-Varrault, B.; Wallington, T. J. Database for the Kinetics of the Gas-Phase Atmospheric Reactions of Organic Compounds. *Earth Syst. Sci. Data* **2020**, *12* (2), 1203−1216.

(67) Clarkson, T. W.; Magos, L. The Toxicology of Mercury and Its Chemical Compounds. *Crit. Rev. Toxicol.* **2006**, *36* (8), 609−662.